Supporting Information

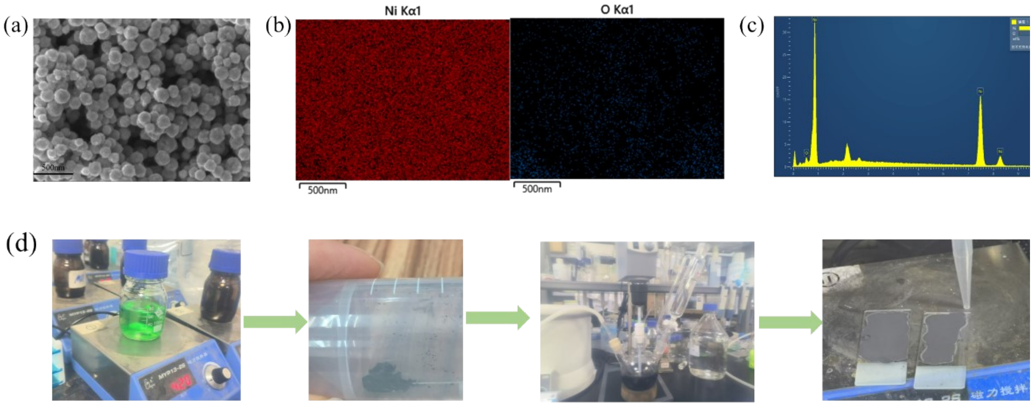

Precursor solution

Ni nanoparticles

reaction solution

Ni @ Sn nanoparticles

Figure S1. Characterization of the synthesized Ni nanoparticles and the fabrication of Ni@Sn nanoparticles. (a) SEM image, (b) EDS elemental mapping, and (c) EDS spectrum of the as-prepared Ni nanoparticles. (d) Fabrication process of Ni@Sn nanoparticles.

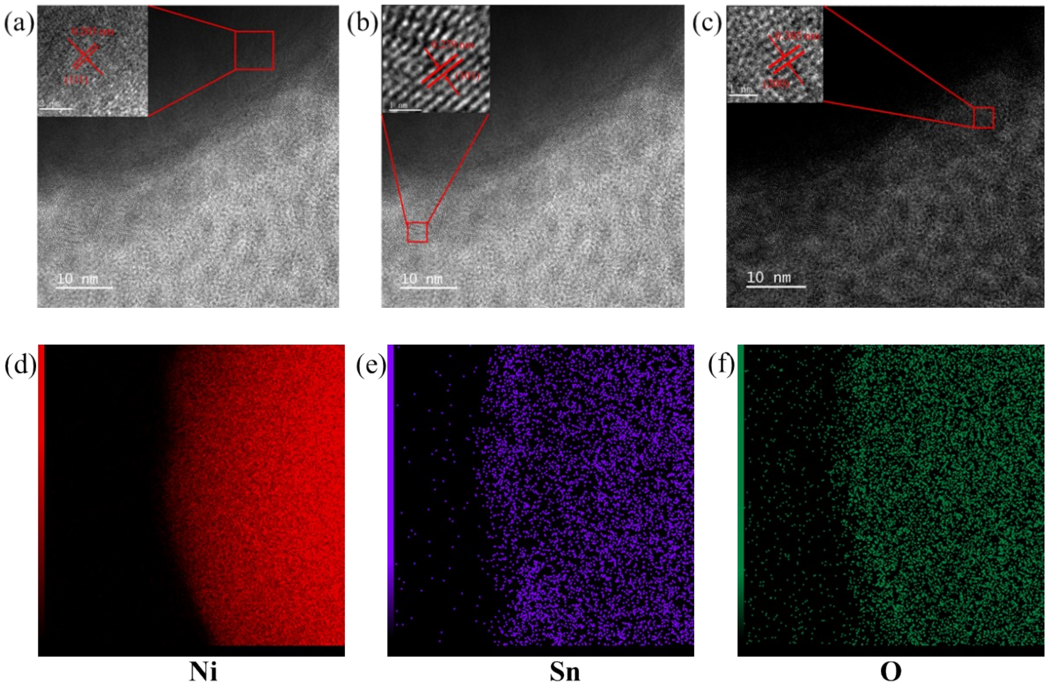

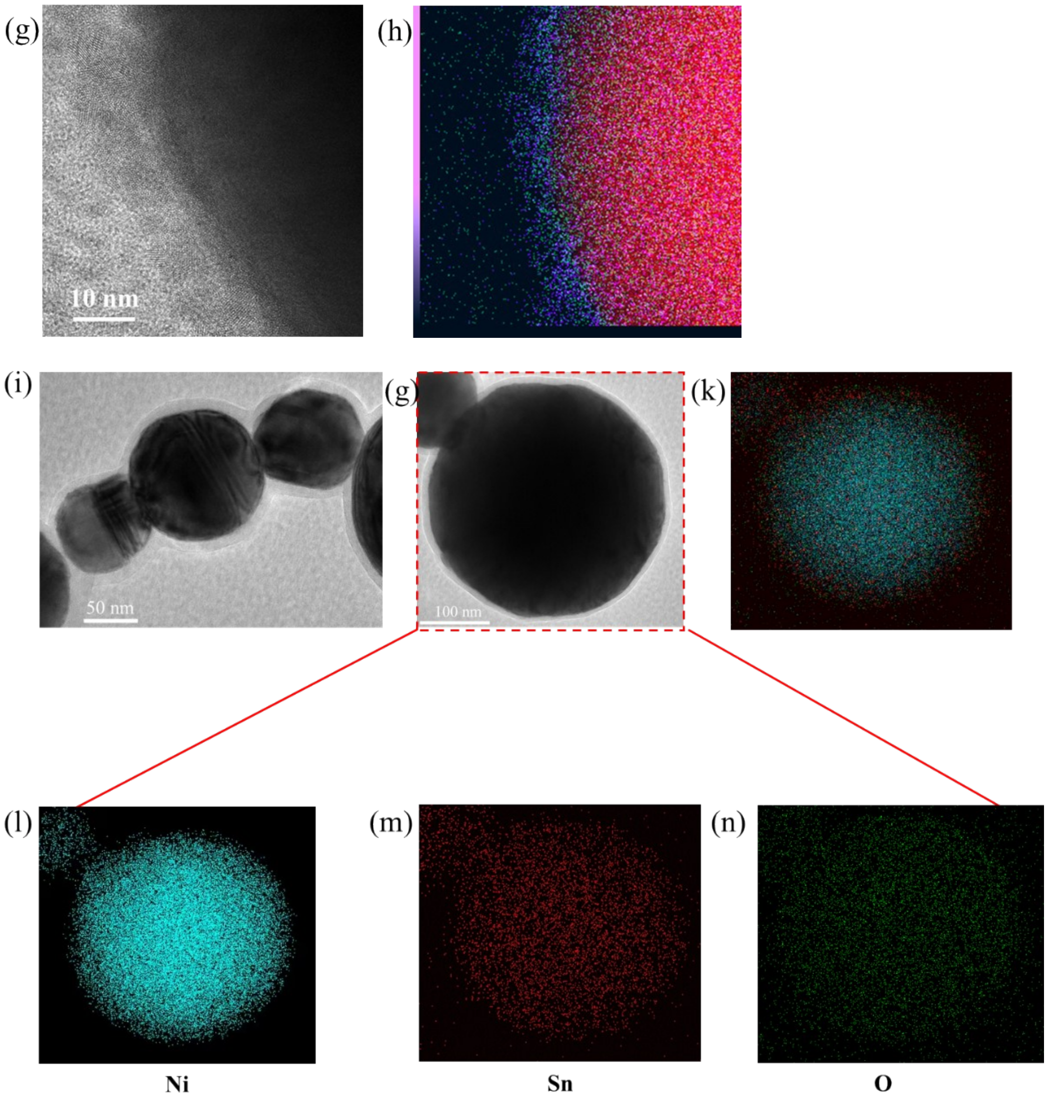

Figure S2. Structural and compositional characterization of the Ni@Sn core-shell nanoparticle. (a-c) High-resolution TEM (HRTEM) images of the representative crystalline regions, (a) Ni core with lattice fringes of 0.203 nm corresponding to the (111) plane, (b, c) Sn shell showing lattice spacings of (b) 0.279 nm and (c) 0.305 nm, indexed to the (101) and (200) planes of Sn, respectively. The insets show the corresponding enlarged views of the lattice fringes. (d-f) EDS elemental mapping images showing the spatial distribution of (d) Ni, (e) Sn, and (f) O atoms. (g) Corresponding TEM image of the scanned area at the nanoparticle boundary. (h) Overlaid EDS mapping image, clearly demonstrating the well-defined core-shell architecture with the Ni core encapsulated by a continuous Sn shell. (i, g) Representative TEM images obtained from different regions showing the consistent core-shell morphology of Ni@Sn nanoparticles. (k) Overlaid EDS elemental mapping showing the spatial core-shell distribution. (l-n) Individual EDS elemental maps of (l) Ni, (m) Sn, and (n) O, respectively.

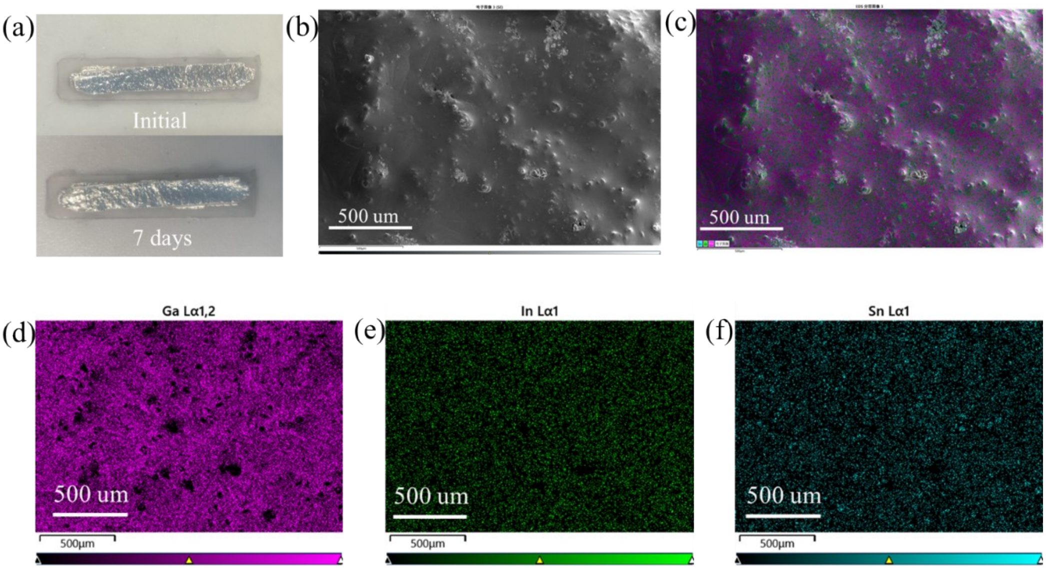

Figure S3. Characterization of the morphological integrity and elemental distribution of Sn particles in Galinstan. (a) Macroscopic photographs of the LM-Sn composite (containing 20 wt% Sn) at the initial stage and after 7 days of storage, showing no significant leakage or phase separation. (b) Cryo-SEM image of the LM-Sn composite after 7 days, illustrating the retention of solid-phase particles within the liquid metal matrix. (c) The corresponding overlaid EDS mapping image highlighting the elemental distribution on the composite surface. (d-f) Individual EDS elemental maps of (d) Ga, (e) In, and (f) Sn, respectively. The concentrated signals in (f) confirm that Sn particles remain as distinct solid phases and do not undergo complete dissolution or homogenization after prolonged incubation.

Calculation of Interfacial Binding Energy

The interfacial binding energy is calculated based on established methodology in computational interface science, defined as follows,

$$\gamma_{Ni/Sn} = \frac{1}{2A}\left(E_{total} - E_{Ni\,slab} - E_{Sn\,slab}\right) \qquad (1)$$

where E_{total} is the total energy of the fully relaxed Ni/Sn interface supercell, $E_{Ni\,slab}$ and

$E_{Sn\,slab}$ represent the energies of the isolated Ni and Sn slabs, respectively, both of which are maintained in the same strained state as they are within the interface supercell. A denotes the interface area, and the factor of 2 accounts for the two equivalent interfaces present in the supercell. The term (E_{total}-$E_{Ni\,slab}$-$E_{Sn\,slab}$) represents the interface formation energy. A negative formation energy signifies that the creation of the interface is an exothermic process. The interfacial binding energy γ is conventionally reported as a positive scalar to quantify the magnitude of cohesion or adhesion strength per unit area. In the following discussion, we focus on the absolute values of the interface formation energy.

Table S1. Computational parameters and results for the interfacial binding energy of the Ni-Sn system.

E_{total} (eV)	$E_{Ni\,slab}$ (eV)	$E_{Sn\,slab}$ (eV)	A (Å^2)	γ_{Ni-Sn} (J/m^2)
-38493.844	-22007.565	-16480.645	23.333	1.93

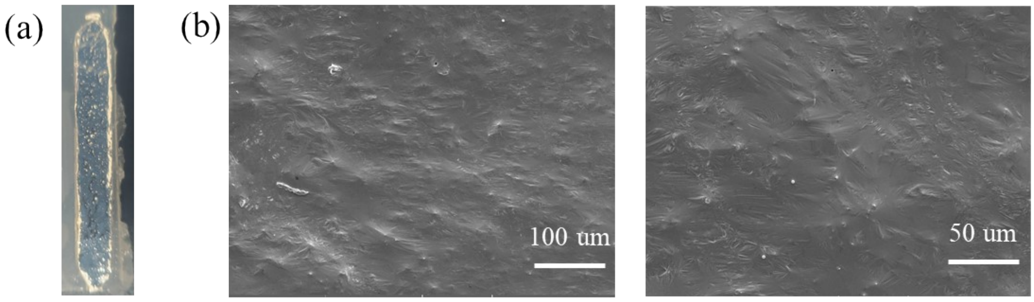

LMNS-10 wt%

LMNS-10 wt%

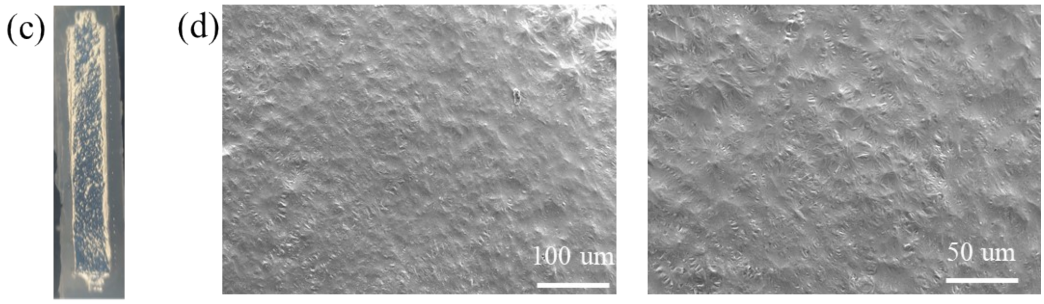

LMNS-20 wt%

LMNS-20 wt%

Figure S4. Characterization of LMNS composites with different mass fractions. (a) Optical image of the LMNS-10 wt% composite. (b) SEM images of LMNS-10 wt% at different magnifications. (c) Optical image of the LMNS-20 wt% composite. (d) SEM images of LMNS-20 wt% at different magnifications.

Theoretical Modeling and Derivation of LMNS-Based Strain Sensors

The strain-sensing mechanism relies on the resistance variations of the conductive LMNS composite deposited on a flexible Ecoflex substrate, where the applied strain is quantified by monitoring the corresponding change in electrical resistance.

To correlate the applied strain with the resistance variations of the LMNS-based circuits, the following assumptions are established: (i) both the LMNS composite and the flexible Ecoflex substrate are considered isotropic and incompressible, ensuring the volume of the composite remains constant during stretching; (ii) the electrical resistivity (ρ) of the LMNS composite is assumed to remain invariant throughout the deformation process; and (iii) the surface tension of the low-modulus Ecoflex elastomer is neglected, assuming the conductive circuit undergoes synchronous deformation with the elastic substrate to ensure consistent electromechanical performance for flexible electronics.

The resistance variation follows the resistance law $R=\rho l/A$, where ρ, l, and A represent the electrical resistivity, length, and cross-section area of the LMNS-based circuit, respectively. The resistance values before stretching R_0 and after stretching $R^{'}$ are defined as follows:

$$R_{G0}=\frac{\rho l_0}{A_0} \tag{2}$$

$$R^{'}=\frac{\rho l^{'}}{A^{'}} \tag{3}$$

here, ρ is the resistivity of the conductive circuit, l_0 and A_0 are the initial length and cross-section area of the LMNS-based conductive circuit, while $l^{'}$ and $A^{'}$ represent the length and cross-section area of the LMNS-based conductive circuit after stretching, respectively.

Assuming the volume of LMNS-based conductive circuit does not change under stretching. Then, we have

$$A_0 l_0 = A^{'} l^{'} \tag{4}$$

By substituting Equation (4) into Equation (3), the resistance after stretching can be obtained as:

$$R^{'} = \rho \frac{l^{'2}}{A_0 l_0} \tag{5}$$

Subtracting the initial resistance value R_{G0} from Equation (5), the resistance change is written as:

$$\Delta R = R^{'} - R_{G0} \tag{6}$$

From Equations (6) and (2), we have $l^{'} = l_0(1 + \varepsilon)$. Then, the relative resistance change can be expressed as a function of the strain *ε*.

$$\frac{\Delta R}{R_{G0}} = \frac{R^{'}}{R_{G0}} - 1 = \left(\frac{l^{'}}{l_0}\right)^2 - 1 = \varepsilon^2 + 2\varepsilon \tag{7}$$

However, when measuring the electrical resistance of the LMNS-based conductive circuit, the measurement value of resistance *R* includes not only the electrical resistance of the LMNS-based conductive circuit, but also the contact resistance R_c between the LMNS composite conductive circuit and the solid conductive Cu wires. Thus, the measured electrical resistance should be expressed as:

$$R_0 = R_{G0} + 2R_C \tag{8}$$

Assuming that the contact resistance $2R_C$ remains constant during stretching, Equation (9) is derived by substituting the expression for ΔR from Equation (7) and the relation $R_{G0} = R_0 - 2R_C$ obtained from Equation (8) into the definition of the actual relative resistance change $\Delta R/R_0$:

$$\frac{\Delta R}{R_0} = (\varepsilon^2 + 2\varepsilon)\frac{R_{G0}}{R_{G0} + 2R_C} = (\varepsilon^2 + 2\varepsilon)\frac{R_0 - 2R_C}{R_0} = (\varepsilon^2 + 2\varepsilon)\alpha \tag{9}$$

where R_0 is the initial measured resistance, and the fitting parameter $\alpha = \frac{R_0 - 2R_C}{R_0}$.

Strain sensitivity is defined as the slope of the resistance change rate ($\Delta R/R_0$) versus strain(*ε*), formulized as GF (Gauge Factor) $= \frac{\Delta R/R_0}{\varepsilon}$. The strain sensitivity of the LMNS-based sensor can be quantitatively assessed by the gauge factor (GF), and the GF (sensitivity) of the sensor can be determined by:

$$GF = \frac{\Delta R/R_0}{\varepsilon} = \alpha(\varepsilon + 2) \tag{10}$$

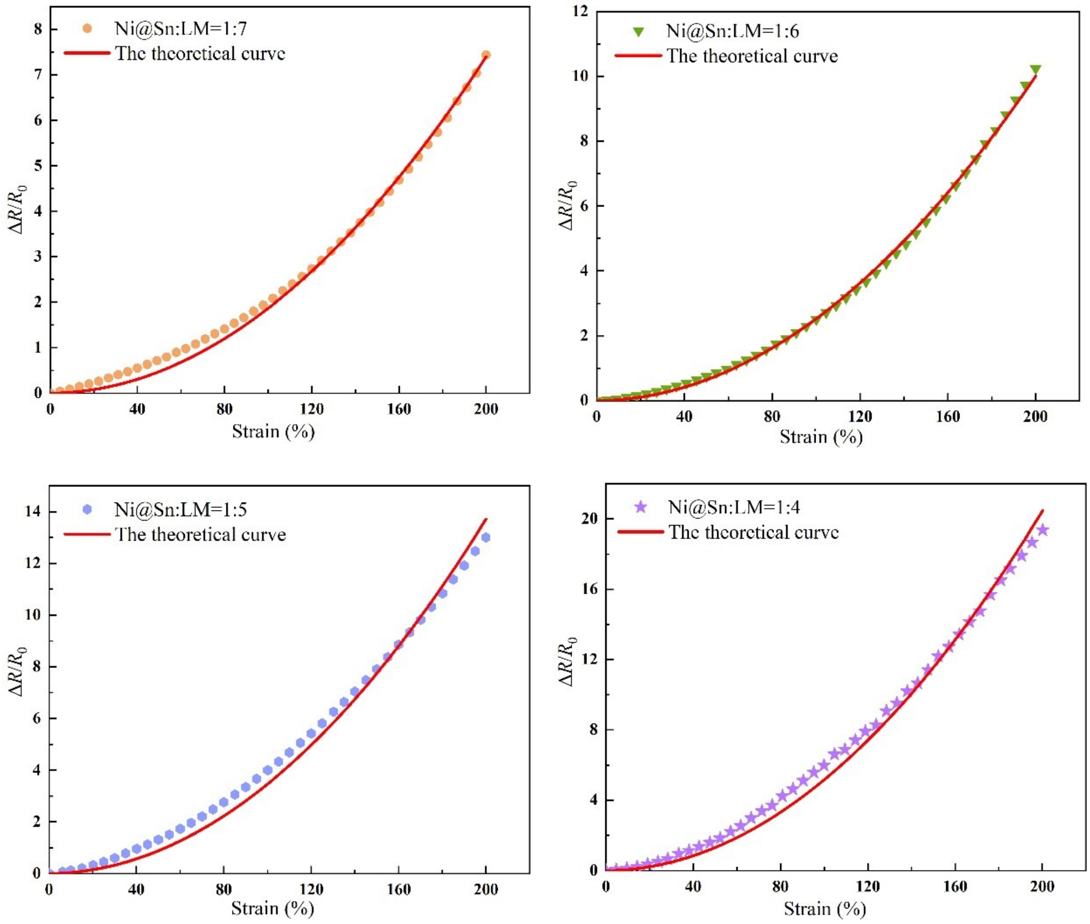

Figure S5 The experimental strain-relative resistance changes and the corresponding fitting curves of the LMNS-based strain sensor with different mass ratios.

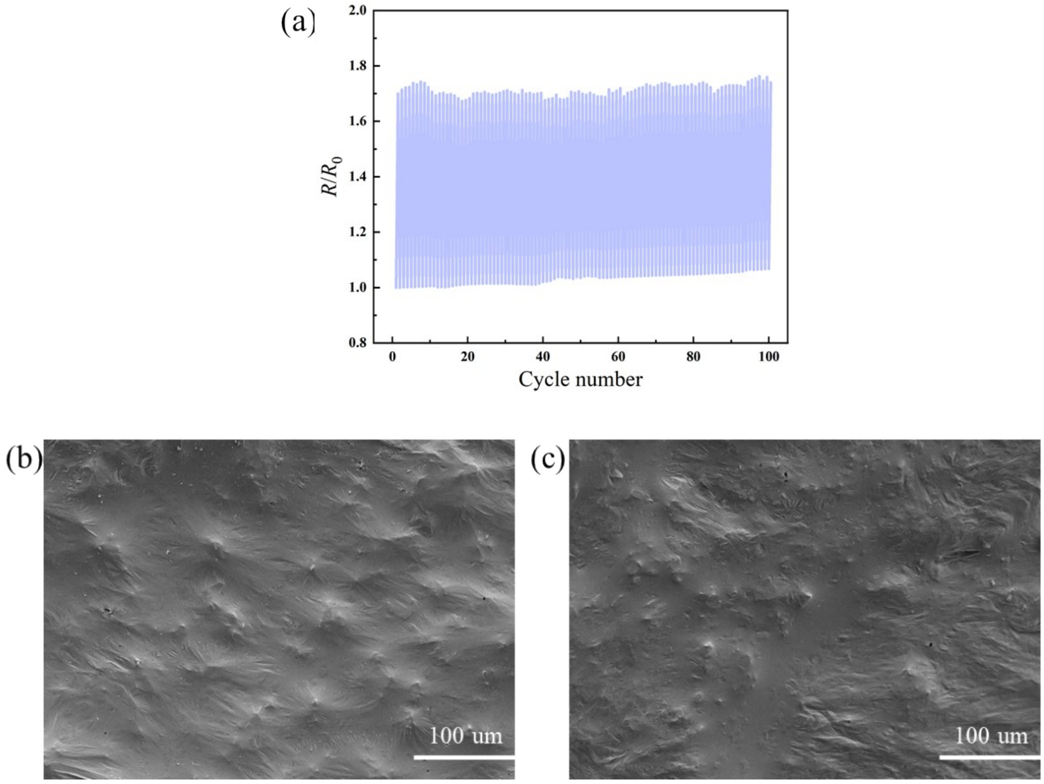

Figure S6. Cyclic electromechanical performance and SEM characterization of the LMNS-15% composite. (a) Relative resistance change (R/R_0) of the LMNS-15% sample during 100 loading-unloading cycles at 50% strain. (b) SEM image of the initial surface morphology of the LMNS-15% sample. (c) SEM image of the surface morphology of the LMNS-15% sample under 50% tensile strain.

Table S2. Comparison of this work's performance with that in the literature.

Conductive material	Methods	Working range (%)	Gauge factor	Ref.
Galinstan	Direct injecting	$0<\varepsilon<140$	2.2	49
EGaIn	Screen printing	$0<\varepsilon<40$	1.16	50
EGaIn	Spraying method	$0<\varepsilon<100$	4.36	51
EGaIn@SiO_2	Physical mixing	$0<\varepsilon<100$	2.27	52
EGaIn-Ni	Physical mixing	$0<\varepsilon<300$	3.2 at 100%	38
EGaIn-CHACC	Ultrasonic mixing	$0<\varepsilon<40$	8.29	53

Galinstan-Ecoflex-Fe	Ultrasonic mixing	$0<\varepsilon<100$	1.91	54
EGaIn-Fe@Fe^{Ga_2O_4}	Chemical modification	$0<\varepsilon<50$	1.56 at 50%	55
Galinstan- Ni@Sn	Chemical modification	$0<\varepsilon<200$	9.1	This work

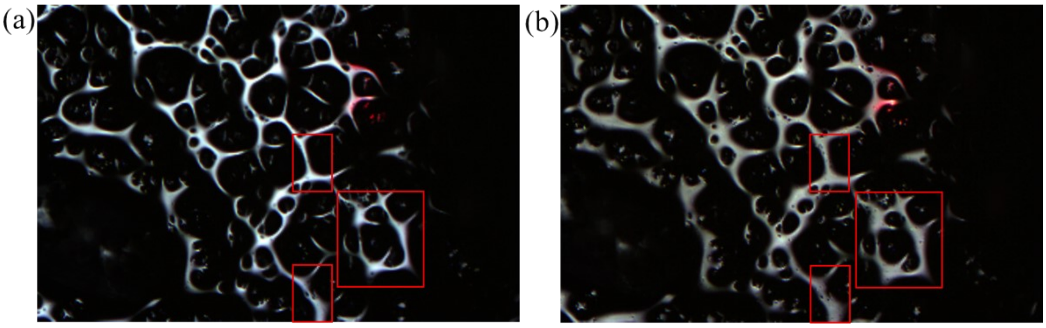

Pristine LMNS (Field OFF)

LMNS under static magnetic field (Field ON)

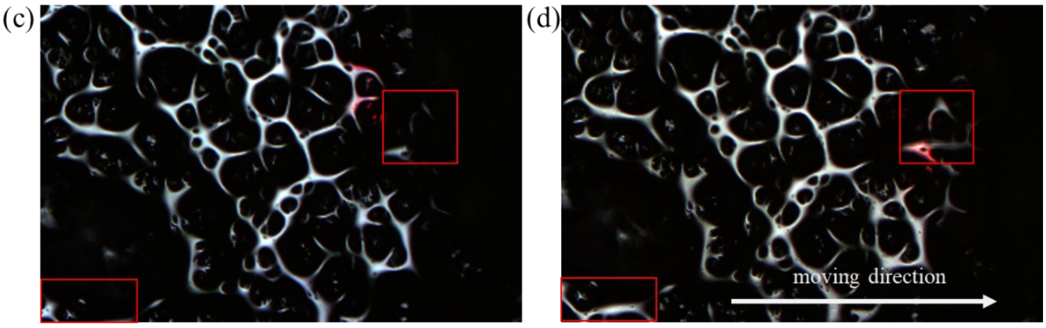

Pristine LMNS (Reference)

LMNS under a moving magnetic field

Figure S7. Optical microscopy images of LMNS under different magnetic field conditions. (a, c) Pristine LMNS without an external magnetic field. (b) LMNS under a static magnetic field, where surface protrusions are observed in the red boxes. (d) LMNS after the movement of a magnetic field, showing local substance accumulation within the red boxes.

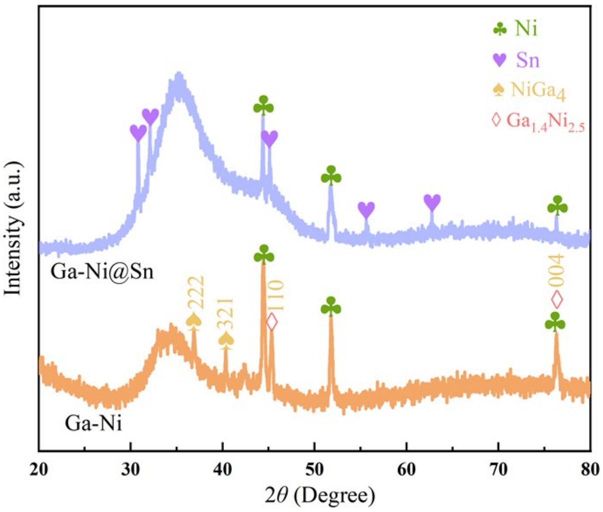

Figure S8. XRD patterns of bare Ni and Ni@Sn particles dispersed in a liquid Gallium matrix.

XRD patterns of the Ga-Ni mixture and Ga-Ni@Sn composite are presented in Figure S8. The emergence of distinct diffraction peaks for intermetallic compounds (IMCs), specifically NiGa$_4$ and Ga$_{1.4}$Ni$_{2.5}$, in the Ga-Ni sample confirms the interfacial alloying between bare Ni and pure Ga. In contrast, the absence of any IMC peaks in the Ga-Ni@Sn sample demonstrates that the Sn shell effectively prevents gallium-induced corrosion, ensuring the stability of the composite in a pure Ga matrix.

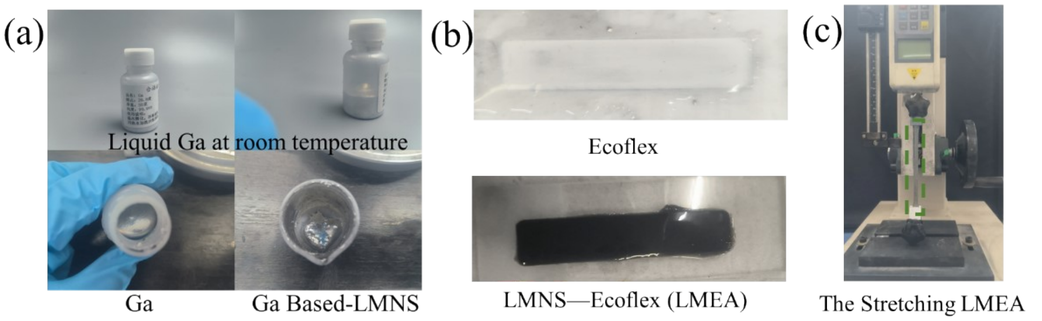

Figure S9. Optical photographs and stretchability demonstration of the LMEA composites. (a) Optical photographs of pristine Ga and Ga-based LMNS at room temperature. (b) Optical photographs of the pure Ecoflex and LMNS-Ecoflex (LMEA) composites. (c) Digital images demonstrating the superior stretchability of the LMEA sample.

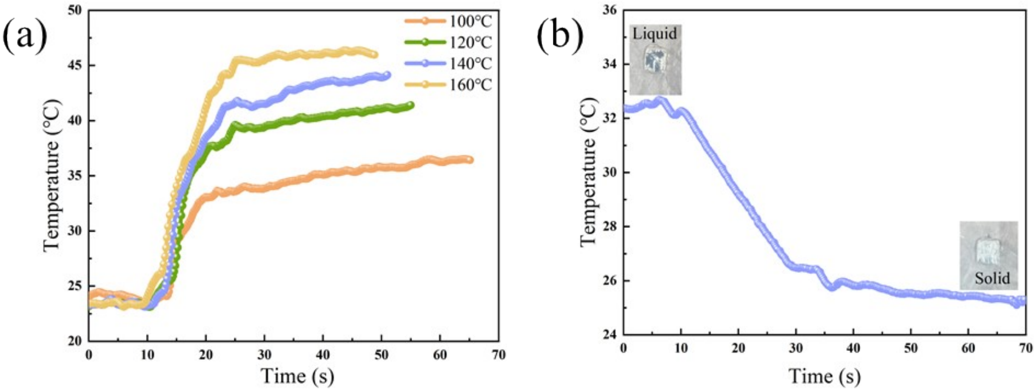

Figure S10. Temperature profiles of the LMNS during heating and cooling processes. (a) Temperature profiles of the LMNS under different heater temperatures (100-160 °C). (b) Cooling curve of the LMNS demonstrating the temperature decrease and the transition from liquid to solid state.

Magnetically controlled LMNS for drug delivery

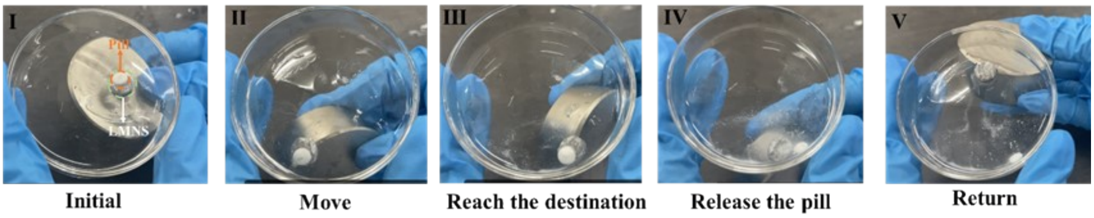

Figure S11. Proof of concept demonstration of the LMNS carrier for targeted drug delivery.

Miniaturized magnetic fluid capable of transferring and releasing cargo is attracting great interest in research communities including for soft robots, drug delivery and environmental pollution treatment. Therefore, to investigate the feasibility of the LMNS for drug delivery application, we designed a proof-of-concept demonstration as illustrated in Figure S11.

As depicted in Figure S11, for this demonstration, a white vitamin tablet is used as the model drug. We pipetted the pill (white vitamin tablet) onto the LMNS composite (stage I) and the pill carrier was fabricated after the curing of the LMNS composite at room temperature for 10 minutes. Then the LMNS pill carrier began to move under magnetic control (stage II), and was guided to the destination (stage III), facilitating the pill release (stage IV). After pill unloading, the LMNS pill carrier could be recalled and magnetically driven to the starting position to await the next task (stage V).

Magnetic self-Healing Electronics Based on LMNS

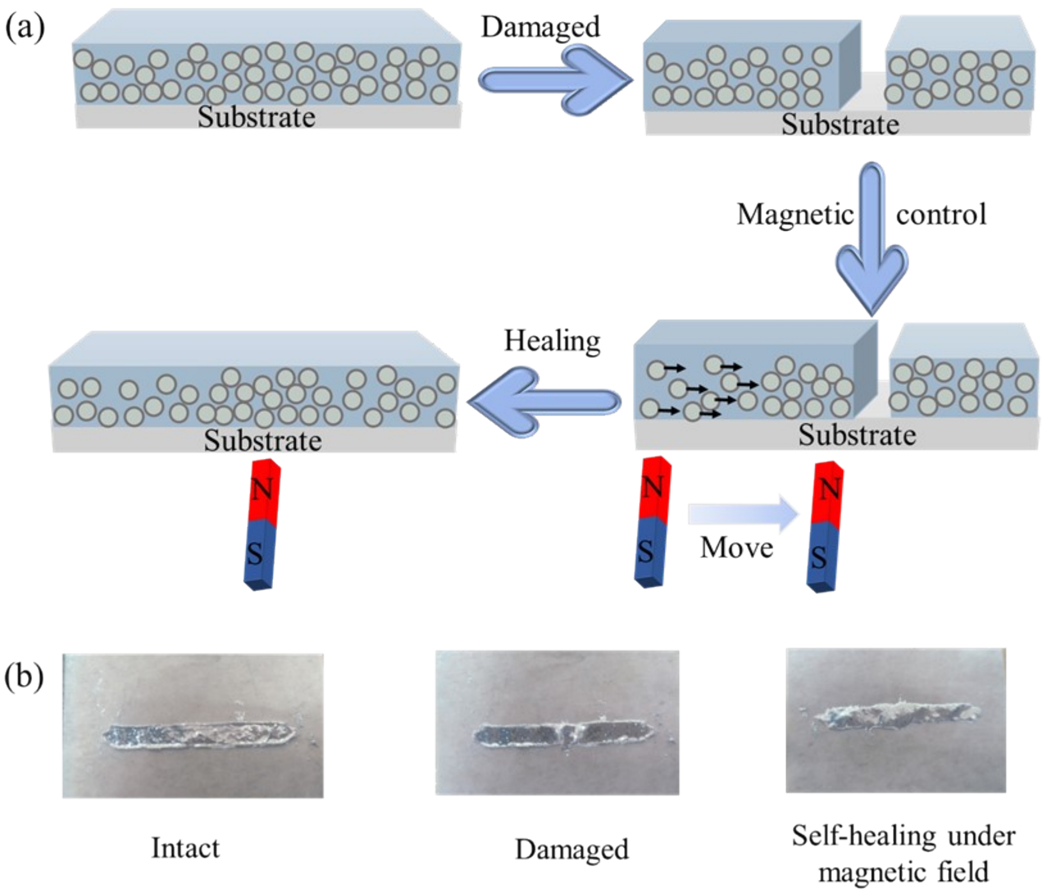

Figure S12. Magnetic self-healing electronics based on LMNS. (a) Schematic illustration of the healing process under a magnetic field. (b) Photographs of the magnetic healing process for LMNS conductive line.

The flexible electronics developed in this paper are mainly composed of two parts, magnetic LMNS circuit and the substrate. Due to the unique properties of the material, the LMNS-based electronics could realize multifunctional magnetic healing performance. Briefly, when a moving magnetic field is applied to the LMNS conductive lines, the Ni@Sn nanoparticles aggregate and carried the Galinstan to fill the mechanical damage gap (Figure S12a).

Figure S12b illustrates the magnetic healing process of LMNS conductive line after mechanical damage. A LMNS conductive line was severed using a blade to simulate a mechanical cut. Subsequently, a magnet was placed beneath the paper substrate to apply a magnetic field. By moving the magnet across the gap, the LMNS paste followed the magnetic attraction to fill the void and achieve the self-healing process. Upon removal of the magnet, the conductive path was successfully restored. Furthermore, the surrounding LMNS paste was recruited by the magnetic force to bridge the crack and reform the circuit.